 doi:10.20944/preprints202110.0024.v1

Article

Fully Metallic Reflectarray for the Ku-band Based on a 3D Architecture

Jaime Velasco, Ignacio Parellada-Serrano, Carlos Molero

Dept. of Signal Theory, Telematics and Communications, University of Granada, 18071 Granada, Spain; jaimevelgar@correo.ugr.es (J.V); parellada@ugr.es (I.P.) cmoleroj@ugr.es (C.M.);
* Correspondence: cmoleroj@ugr.es

Abstract: This document presents the design and manufacture of a reflectarray (RA) antenna for the Ku-band, based on a fully-metallic 3D architecture. The reflectarray unit cell is formed by a square-shaped waveguide section ended in a short circuit, that is the reflectarray back ground plane. Each cell has the ability of configuring the phase of its own reflected field by means of resonators perforated on the walls of the cell waveguide section. The resonator-based waveguide cell introduces the 3D character to the design. The geometry of the resonators and its size variation introduces the phase behaviour of each cell, conforming the radiation pattern of the reflectarray. This design explores the potential of phase value truncation (6 states and 2 states), and demonstrates that proper pattern results can be obtained with this phase truncation.

Keywords: reflectarray, 3D architecture, resonator-based waveguide cells, Satellite communications, Ku band

1. Introduction

The increasing requirements in antennas for broadcast and telecommunications are becoming challenging due to the emergence of novel technologies and the fast development of new fabrication techniques. Especially the arrival of 5G communications standard and the establishment of the operating bands at millimeter frequencies [1]. Microwave devices operating at these frequencies finds several restrictions associated with size, weight, fabrication constraints or a relevant increase of losses [2].

An essential element in current satellite infrastructures are beamforming networks [3]. Parabolic antennas has widely covered this task, especially beam-redirection and focusing. However they have intrinsic drawbacks as very large dimensions, bulkiness and heavy weight [4], and their use is not suitable in several scenarios. The common alternative to parabolic reflectors are phased array antennas [5–7,9]. Phased array antennas are, in contrast to the parabolic ones, planar devices. The are formed by distributions of individual emitters whose field amplitudes and phases are externally controlled. The global radiation pattern of a phased array antenna is obtained by superposing the contribution of the individual fields radiated from each emitter [8].

Phased arrays exploit the ability to steer a radiation beam into a desired direction. They may include the feeding network in the device architecture, generally supported on complex circuitry. For instance they require the use of power dividers [10], phase-shifters [11], or active elements [12]. Reflectarray (RA) antennas are a less complex solution of phasing systems, being lightweight, low-profile, and showing adaptability [4,13]. To the author's knowledge, the first RA design was reported in the sixties by D. Berry et al [14]. At first, RA prototypes were typically based on metallo-dielectric structures [15–18], fabricated via standard PCB techniques. However thanks to the growing of novel 3D-printing fabrication techniques, RA based on fully-dielectric [19] and fully-metallic designs [20] have emerged. In particular, fully metallic RAs are being demanded beyond the K- and Ka-bands, where dielectric losses stop being negligible. Examples of

Preprints (www.preprints.org) | NOT PEER-REVIEWED | Posted: 1 October 2021 doi:10.20944/preprints202110.0024.v1

fully metallic RAs have already been proposed and published in the literature, as those reported in [21,22].

The fast and recent development of 3D-printing techniques introduces the possibility of innovating in the shape of the cells [23]. For instance 3D architectures arise as elegant solutions thanks to the additional degrees of freedom they introduce [24]. The 3D character of a given cell is forced by including resonant elements along the axial (or propagation) direction [25,26]. 3D cells have the ability to control independently different field components. Paradigmatic examples were reported in [27,28], where fully-metallic cells with 3D architectures were employed to design dual-band/dual-pol devices, combining both 3D architecture and full-metal cavities. These type of cells are promising since they are mechanically self-consistent, and no help of support is needed.

In this work we present a fully-metallic RA based on the ideas reported in [28]. Though our final goal is the conception of a RA operating at millimeter frequencies, in this document we focus in a Ku-band prototype with the aim of obtaining a first proof of concept. The RA is supported on a metallic metasurface consisting of distributions of square waveguides. The structure is illuminated by a normally-oriented plane wave. The waveguide walls are perforated with resonators, whose role is to modify/control the individual phase of the reflected wave associated with each of the waveguide cells. Under these circumstances two kind of RAs will be presented. First, a RA formed by a discrete distribution combining 6 possible phase states; and a second case considering binary cells, highly used nowadays because of their easy implementation [29].

This document is organized as follows: Section II describes the principle of operation in terms of the unit cell. Section III shows the performance of the cell for different geometries. Section IV includes a numerical validation of the concept, for both prototypes with 2 and 6 possible states. In section V we explain the fabrication process and the experimental results obtained in the laboratory. Finally, the conclusions of this work are drawn in Section VI.

2. Brief description of the unit-cell type

The structure under consideration in the present manuscript is a Frequency Selective Surface (FSS) based on a full-metal design. As shown in Fig. 1(a), it consists of a two-dimensional arrangement of classical square waveguides (cells). The dimensions of the cells are such that no propagating modes are excited at the operation frequency ($P \leq \lambda_0/2$ with λ_0 being the wavelength in vacuum). Instead, only evanescent modes will be present inside the cell. A ground plane is placed at the bottom of the cell, in order to force full-reflection response.

Perforations with *special shape* are done on the waveguide walls with the purpose of controlling the field behavior inside the cell. These perforations actually play the role of slot resonators, which modify drastically the electromagnetic response of the cell at frequencies close to their own resonance frequency. Two main resonator-shapes are proposed, illustrated in Fig. 1(b)-(c). Fig. 1(b) shows a *C-shaped* perforation. Similarly, a *S-shaped* resonator has been perforated on the wall of the cell in Fig. 1(c). Their effective length L is assumed to be long in comparison with the waveguide dimensions.

The resonators are extended along the propagation (axial) direction z, giving a 3D character to the structure. 3D architectures enhance certain typical properties of 2D FSSs designs. The inclusion of resonant elements along the propagation direction introduces an additional degree of freedom, very useful for design and optimization processes. Moreover, the control of the vertical and horizontal field-polarizations (V- and H-pol, respectively) can rigorously be decoupled. In this sense, the resonators on the walls inside the YZ-plane manipulate V-pol and are completely opaque for H-pol. The structure here proposed is optimal for V-pol incidence. More information about this issue is reported in [28].

Preprints (www.preprints.org) | NOT PEER-REVIEWED | Posted: 1 October 2021 doi:10.20944/preprints202110.0024.v1

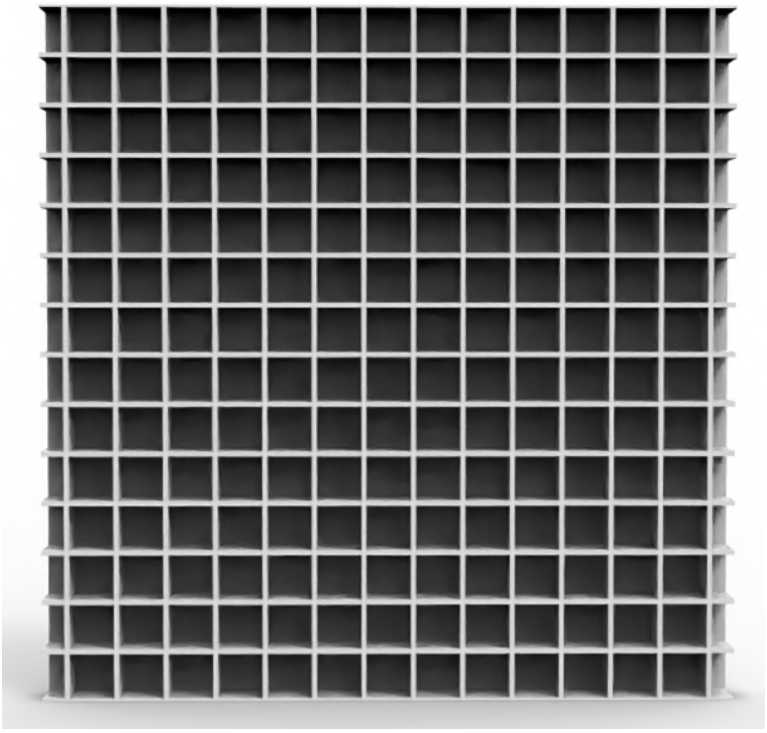

(a)

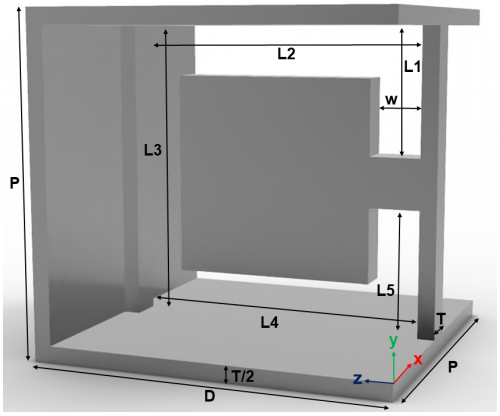

(b)

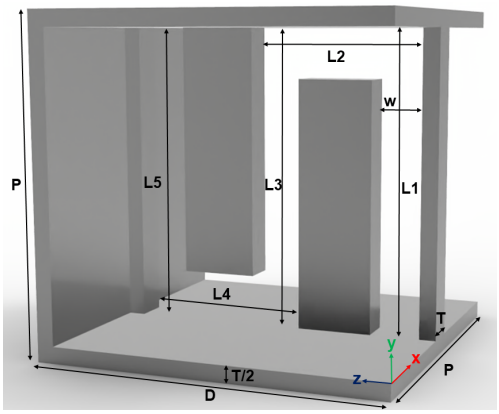

(c)

Figure 1. (a): Array 14x14 of square waveguides. (b): Unit-cell type with C-shaped resonator on the wall and dimensions. (c): Unit-cell type with S-shaped resonator on the wall and dimensions. The length of the slot perforations is calculated as $L = L_1 + L_2 + L_3 + L_4 + L_5$.

3. Performance of the unit cell. Choice of the resonant element

The phase of the reflection coefficient associated with a particular cell is manipulated in terms of the resonant frequency of the resonator. It is well known that in the RA-design context the role of each cell is to provide the correct phase shift to re-direct the incident beam to a desired (different) direction.

In order to study and analyze the phase behaviour of each cell as a function of frequency, we must carry out a detailed study of the configuration of the resonator employed. The process involves modifying the geometry of the resonator so that it becomes smaller and smaller but always maintaining the same width value w between its edges. To do this, we first define the effective length $L = L_1 + L_2 + L_3 + L_4 + L_5$ of

Preprints (www.preprints.org) | NOT PEER-REVIEWED | Posted: 1 October 2021 doi:10.20944/preprints202110.0024.v1

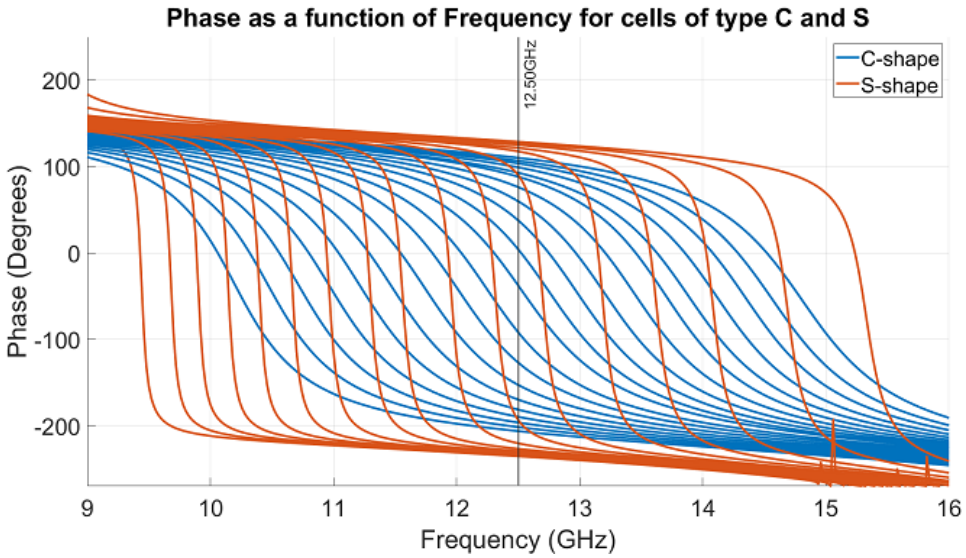

(a)

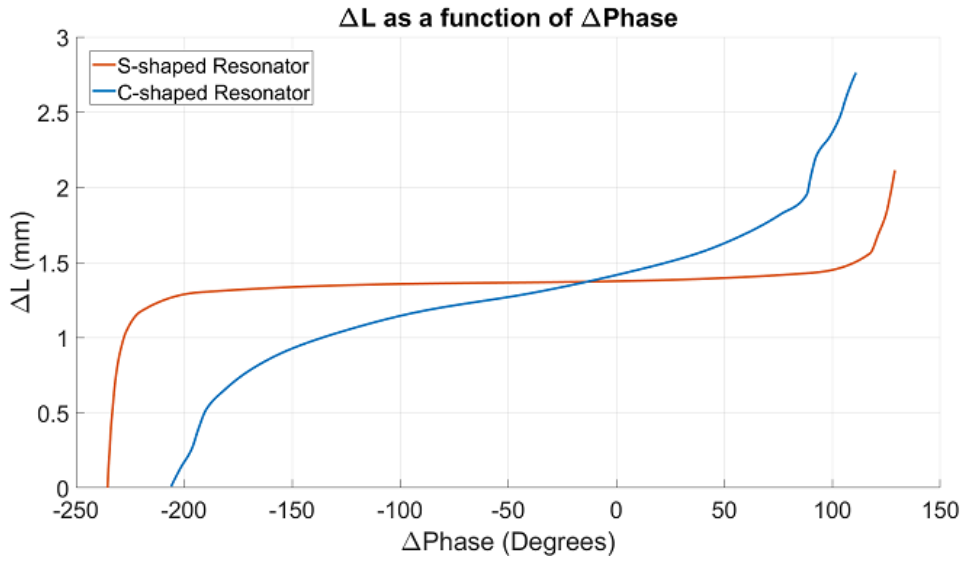

(b)

Figure 2. (a): Phase versus frequency for cells with C-shaped and S-shaped resonators. (b): ΔL versus ΔPhase for S-shaped and C-shaped resonators.

the resonant element. In each iteration we reduce this parameter so that, consequently, a phase curve is obtained, which shifts in frequency as we shorten the resonator.

The study of the phase is realized by computing the S_{11}-parameter of the cell when it is illuminated by a V-polarized plane wave. This study is focused on the Ku-band, specifically at frequencies close to 12.5 GHz. Though no propagating modes are excited inside the cells, the dominant (evanescent) mode is the TE_{10}, whose electric field is oriented on the $\hat{y}$-axis and is the responsible of excitation of the resonances. By modifying the dimensions of the resonator, the phase of the reflection coefficient can be controlled. A specific resonator geometry is characterized by a specific phase curve.

Fig. 2(a) illustrates the phase variation as a function of frequency, for C- and S-shaped resonators. The curves have been obtained by the use of the electromagnetic solver CST. Different curves, each associated with a particular geometry of the resonators, are appreciated. The first graphical difference that we observe corresponds to the slope of the curves of both resonators, being much greater for the S-shaped resonator, which

Preprints (www.preprints.org) | NOT PEER-REVIEWED | Posted: 1 October 2021 doi:10.20944/preprints202110.0024.v1

implies a greater phase change in a smaller range of frequencies. Additionally, taking the central frequency of the configuration as a reference (12.5 GHz), small variations can be appreciated on the C-shaped resonator geometry, corresponding to small phase shifts at the reference frequency. As it can be noticed, S-shaped resonators are more sensitive, providing a stronger shifting even for small geometry variations. Therefore, considering the reference frequency at 12.5 GHz, greater phase variations are given with S-shaped slots while smaller variations are associated with the C-shaped ones, corresponding to smaller phase shifting.

The dependence between the geometry variation and the phase shift is clearer plotted in Fig. 2(b). The geometry variation is denoted by ΔL, whereas the phase shift is identified as ΔPhase. The way to obtain these curves is straightforward thanks to Fig. 2(a). It is done by taking separately all the cut-off points of the phase curves, both of the C- and S-shaped resonators, with the vertical line marking the frequency of 12.5 GHz, that corresponds to the center frequency of the reflector. A soft interpolation has been applied to the curves in order to achieve greater smoothing.

This graph gives us useful information about the phase variation obtained when we modify the effective length L. Analyzing in detail the behavior of these curves, we observe a very similar trend although with a different slope. For the final design of our reflective structure we will take into account two different areas: on one hand, the blue curve (corresponding to the C-shaped resonator) for the central cells, and the orange curve (corresponding to the S-shaped resonator) for the outermost cells. Since the blue curve (C shape) has a bigger slope, greater phase jumps are obtained as we reduce the geometry of the resonator. This is not the case of the S-shaped resonator because a very small change in L (specially from $\Delta L = 2.5$ mm to $\Delta L = 1.35$ mm) causes a large phase jump. It can also be inferred that both kind of resonators are necessary in order to cover an almost 360^o-range. C-shaped resonators cover the *central* area, from -200^o to 100^o approximately (300^o phase span) whereas the *external* area is covered by the S-shaped ones. This allows us to obtain a greater phase variation and to be able to reach the full range very close to 360^o.

4. Reflectarray design: numerical validation

The design plots in the previous section illustrate that the combination between C- and S-shaped perforations practically covers the 360^o-phase range necessary to design a RA. At this point, and for fabrication purposes, we will restrict the phase gradient of our RA to a set of discrete values. On the one hand, a gradient formed just by 6 possible states, whose corresponding phase values are defined by the following relation:

$$\frac{n\pi}{3}, \qquad n \in [0,5] \tag{1}$$

On the other hand, a simple design based in just two phase-states: 0 and π, which will be encoded as 0 and 1, respectively. This is the so-called binary cell.

The design and optimization of the RA is realized according to the scenario shown in Fig. 3. A standard WR-75 horn antenna feeds the RA and is placed at 15 cm from it. This distance is optimal to reduce the spillover. The RA is a 14x14-cells panel with periodicity $P = 10.53$ mm. Ray-tracing approximation is employed to estimate the phase arriving to each of the cells.

The total phase in each cell is equal to the phase of the incident field (due to the propagation from the feed) plus the phase-shift introduced by the own cell. In this sense, the phase shift required at each element to re-direct the incident field is given by the following expression [4]:

$$\begin{gathered}\varphi_{nm} = k_0\left(d_{nm} - [x_n\cos(\varphi_b) + y_n\sin(\varphi_b)]\cos(\theta_b)\right) \\ n, m = 1, ..., 14\end{gathered} \tag{2}$$

Preprints (www.preprints.org) | NOT PEER-REVIEWED | Posted: 1 October 2021 doi:10.20944/preprints202110.0024.v1

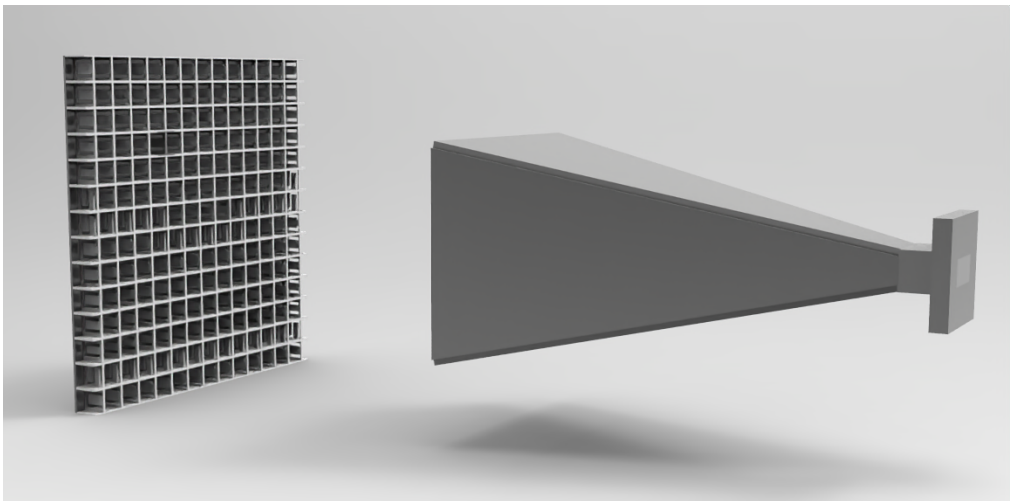

Figure 3. Scenario simulated in CST. The horn feeds the RA from a distance of 15 cm. Structure parameters of the cells in the RA: $P = 10.53$ mm, $T = 0.5$ mm, $D = 10$ mm.

where (x_n, y_m) are the coordinates of the position of the nmth RA-cell, k_0 is the wavenumber in vacuum, and d_{nm} is the distance from the phase center of the feed to the nmth RA-cell. The parameters θ_b and φ_b denote the outgoing polar and azimuthal angles respectively, namely, the pointing direction of the steered beam.

For the sake of simplicity, and as proof of concept, two different pointing angles have been chosen: $\theta_b = 20^o$ and $\theta_b = 35^o$ with $\varphi_b = 0^o$. Assuming first a 6-states phase distribution, the phase-shift value satisfying (2) is approximated to the nearest phase-value in (1). The 14x14-panels for $\theta_b = 20^o, 35^o$ are plotted in Fig. 4(a) and Fig. 5(a), respectively. The corresponding radiation diagrams associated with these panels are plotted in orange line in Fig. 4(c) and Fig. 5(c) respectively. The main lobes are exactly at the desired angles, with a gain of 22.5 and 22.6 dB and a side-lodes level (SLL) of 12.5 and 11.8 dB respectively.

The RA based on binary cells has been optimized by using a Genetic Algorithm since an ad-hoc truncation can result in big phase errors. Specifically, NSGA-II is employed to reach our goal. Non-dominated Sorting Genetic Algorithm, NSGA-II [30], has been used, which is a multi-objective algorithm that has been applied in some of our previous jobs [31]. The optimization process is initialized with a random set of solutions, each one with 14^2 binary variables (0/1). The selection operator utilized is Binary Tournament, while the recombination (also known as crossover) consists in the exchange of random subzones of the phase configuration. In this way, we provide diversity among the solutions, which is key for the algorithm to not stall. Finally, the mutation operator just flips the value of a single bit, from 0 to 1 or vice versa. Previously, we tried to flip a group of bits, but it prevented the algorithm to converge completely. The crucial component of a GA is the fitness function to optimize. Although this algorithm is multi-objective, in this functionality that we call beam steering, only one objective can be established. Thus, we will maximize the gain of the structure at the desired pointing direction.

We can observe in Fig. 4(b) and Fig. 5(b) the 14x14 phase-panel obtained for this case. As expected, the RA has gained in simplicity. It is worth remarking that the phase evolution follows a similar tendency in both cases, simulating a sort of partial rings. The phase diversity is, as expected, richer in the 6-states case. The simplicity of the 1-bit RA is manifested in the results plotted in blue curve in Fig. 4(c) and Fig. 5(c). However, the gain decreases down to 20.8 and 20.7 dB, whereas the SLL increases up to 15.5 and 15.4 dB respectively.

Finally, the scenario in Fig. 3 has been simulated by the commercial software CST. The RA choice is the one with 6 phase-states. The phase distribution in Fig. 4(a) and Fig. 5(b) are implemented in the RA with the help of the design plots in Fig. 2(a)-(b). The

Preprints (www.preprints.org) | NOT PEER-REVIEWED | Posted: 1 October 2021 doi:10.20944/preprints202110.0024.v1

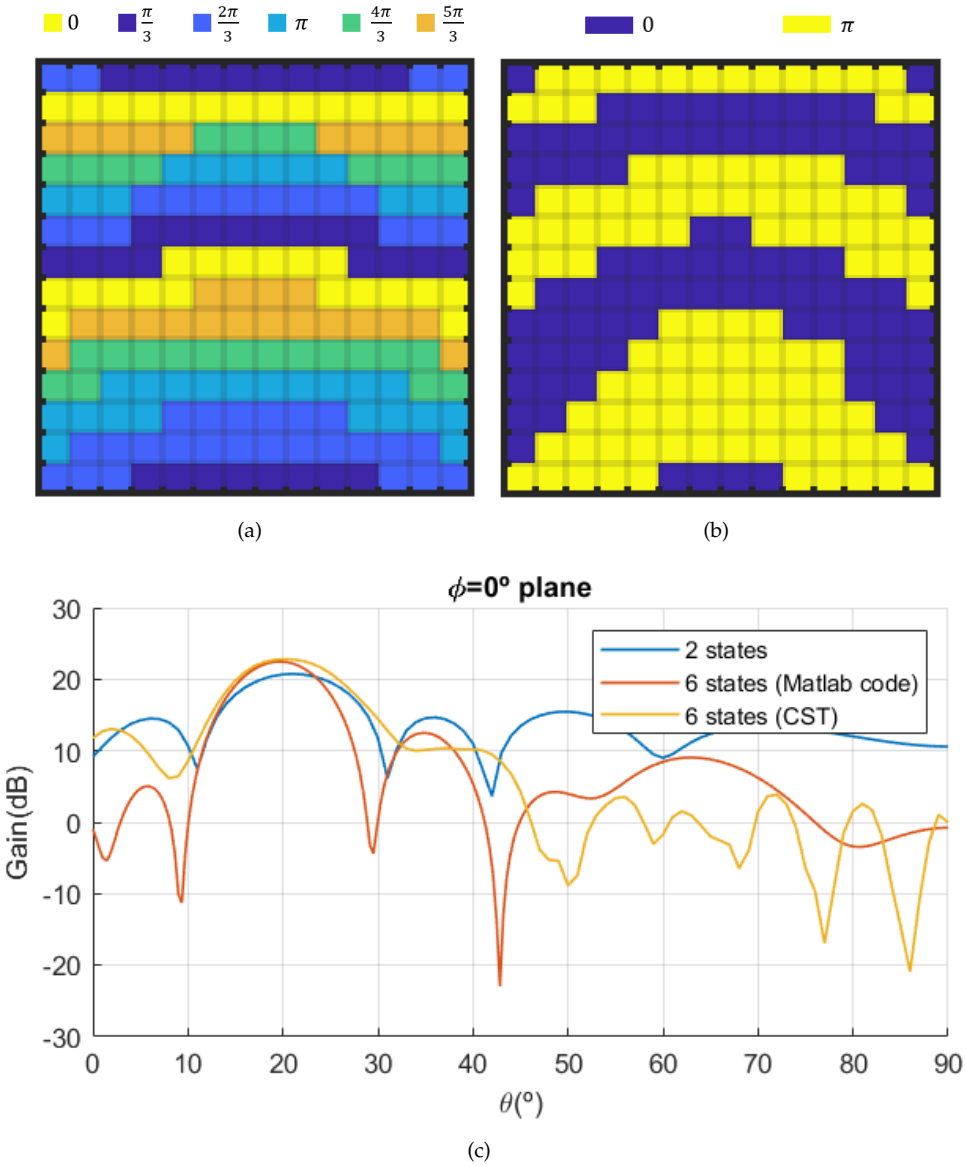

Figure 4. (a): phase arrangement considering 6 states. (b): phase arrangement considering 2 states. (c): Radiation pattern, beam direction: $(\varphi,\theta)=(0,20)^{\circ}$.

results of the simulation are also plotted in Fig. 4(c) and Fig. 5(c) (yellow curves). Minor differences are appreciated due to the avoidance of possible mutual coupling among cells at the designing process. The SLL is otherwise still acceptable, with differences of more than 10 dB with respect the main lobe maximum.

5. Manufacturing and experimental validation

Once the design is optimized and completely adjusted to fulfill the requirements, the structure is manufactured. A 14x14 array prototype has been fabricated. As a proof of concept, we have decided to focus on the 6-states RA operating for $\theta = 20^{\circ}$. The manufacturing process has been carried out thanks to the manufacturing facilities of the SWAT group of the University of Granada. The process implies accurate 3D stereolithography, consisting on the construction of the structure layer by layer by a photochemical process. The material is a resin characterized by $\varepsilon_r = 2.55 - j0.0612$. Since the dimensions of the entire RA are larger than recommended by the 3D printer, it was split and printed in 9 individual pieces. Each of these individual pieces consisted of arrangements of 3x3 or 4x4 cells. Additional supports were needed in order to guarantee

Preprints (www.preprints.org) | NOT PEER-REVIEWED | Posted: 1 October 2021 doi:10.20944/preprints202110.0024.v1

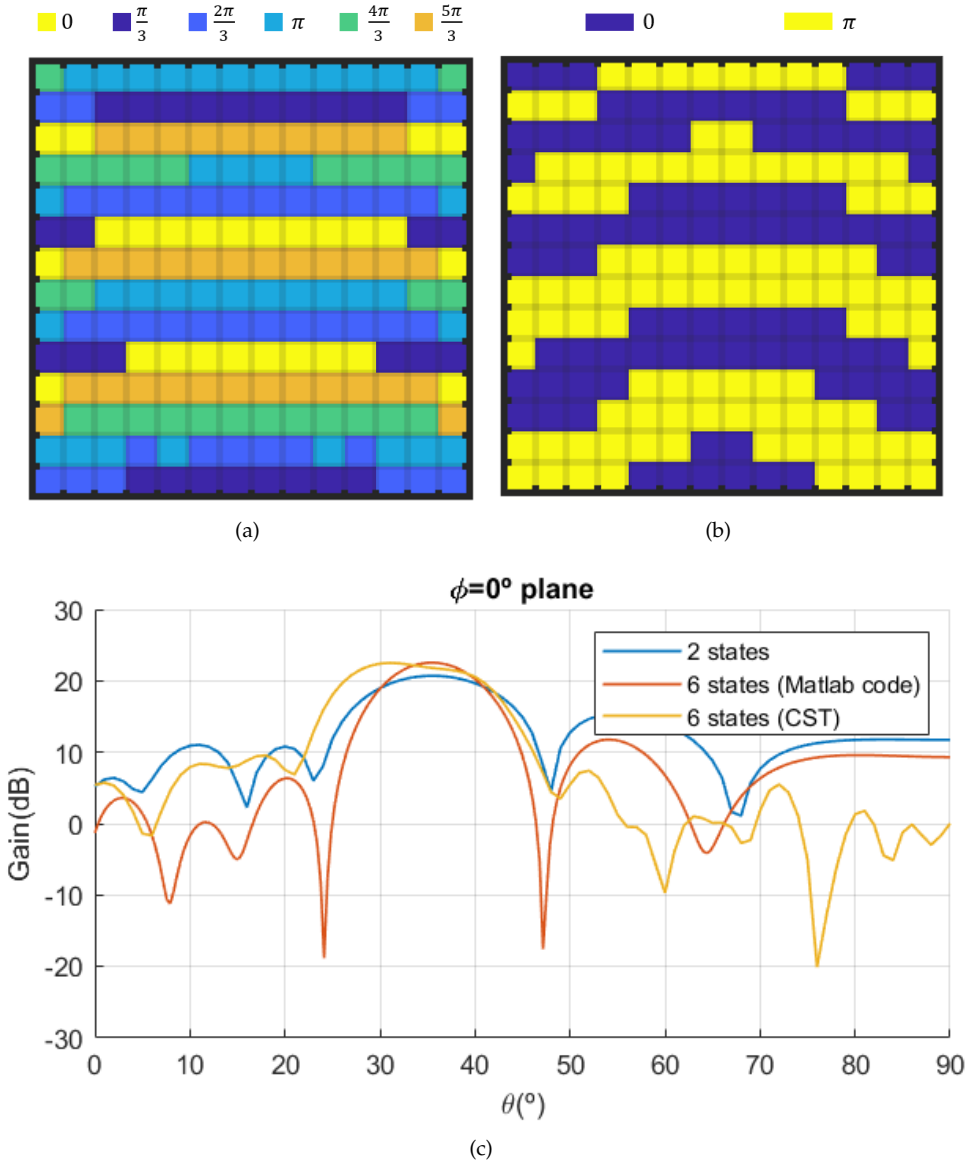

Figure 5. (a): phase arrangement considering 6 states. (b): phase arrangement considering 2 states. (c): Radiation pattern, beam direction: $(\varphi,\theta)=(0,35)^{\circ}$.

the self-robustness of the pieces during the fabrication process. Fig. 6(a) shows the 9 pieces including the supports, which are basically very narrow dielectric bars. These

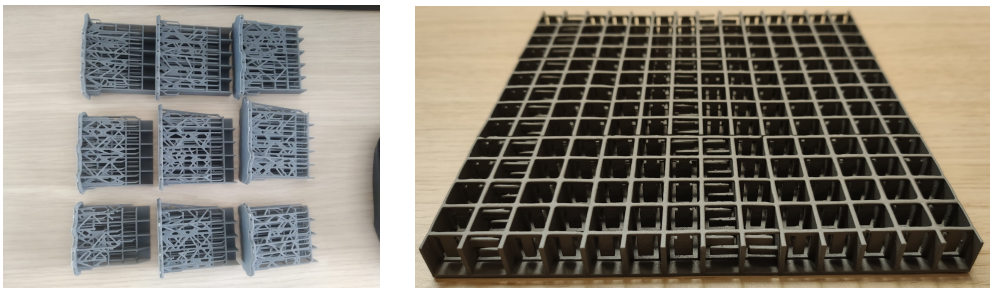

Figure 6. (a): Photo of the individual pieces including the supports. (b): Photo of the final RA prototype. The S- and C-shaped resonators can easily be visualized.

Preprints (www.preprints.org) | NOT PEER-REVIEWED | Posted: 1 October 2021 doi:10.20944/preprints202110.0024.v1

supports are carefully removed by using special scissors. After that all the pieces are glued together, giving rise to the entire RA. Finally, the metallization is realized by using a commercial conductive ink. Fig. 6(b) shows a detailed view of the final prototype. The presence of the ink can be inferred from the darker color of the structure.

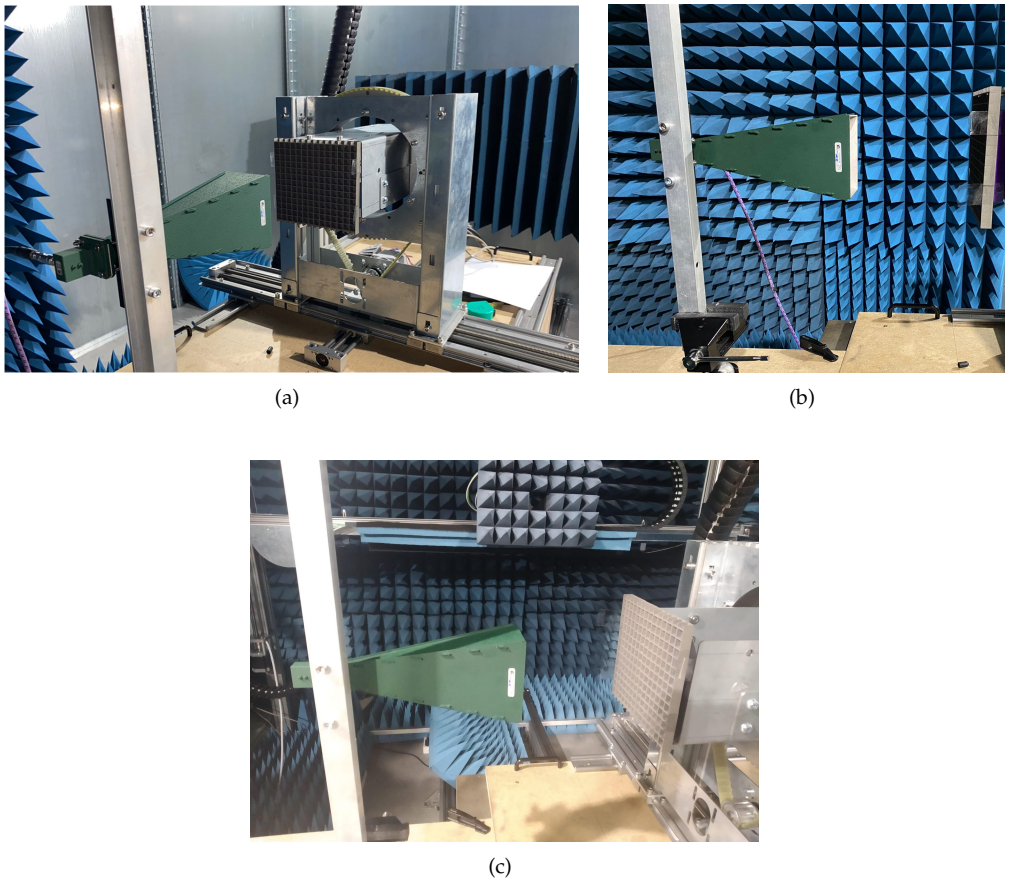

(a) (b)

(c)

Figure 7. RA Antenna prototype mounted in its final configuration (a and b), and (c) measuring setup at the antenna measuring facility of the SWAT Group at the University of Granada.

The structure has been mounted in its setup with the feeder located at the defined distance of 15 cm and measured at the mmWave antenna measuring facility of the SWAT Group at the University of Granada. The RA setup can be seen in Fig. 7(a) and 7(b), while the measuring setup in the measuring system is depicted in Fig. 7(c). The prototype is finally characterized in terms of its radiation pattern in the vertical plane. The pattern measurement is shown in Fig.8, having the center working frequency at 12.7GHz. This yields a frequency shift of 0.2 GHz with respect the theoretical results. The position of the main lobe is approximately situated at the expected angle. There exist a small angular shift towards higher angles. Additionally, the secondary-lobes level is larger than expected from the simulations. It oscillates between -4 and -10 dB in the region close to the main lobe position. This disagreement is important since it reduces considerably the efficiency of the RA. The source of inaccuracy is clearly the fabrication process. The structure is actually challenging from the printing-process point of view. As we explained above, it was split into 9 sections. When the pieces are put together, small misalignments appear among all of them. Furthermore, the metallization via ink must be carefully taken into account. It is very important to metallize all the structure. In the resonator regions the conductive ink may not reach all the corners, reducing the efficiency of the resonator (longer or shorter than expected). Finally, the process of removing the additional supports is very cumbersome. This task is done manually. Some portions of the supports may rest in the structure, affecting the phase

Preprints (www.preprints.org) | NOT PEER-REVIEWED | Posted: 1 October 2021 doi:10.20944/preprints202110.0024.v1

shifting and the final far-field pattern. It is worth mentioning this RA is the first structure manufactured in our group. Now we are refining the technique and we expect to have better prototypes in the near future. We are also exploring how to metallize with copper. The results reported in this paper encourage us to continue.

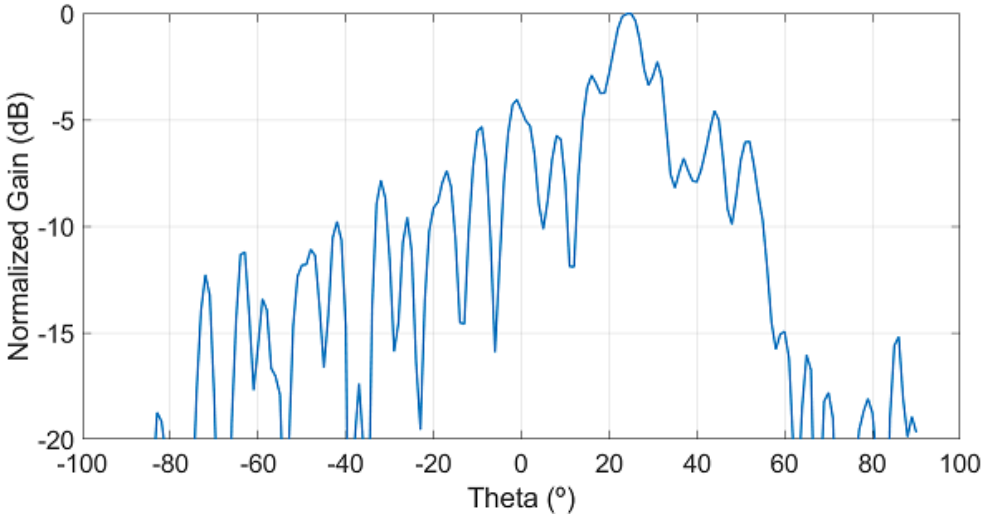

Figure 8. Radiation pattern in the vertical plane. Best result obtained at 12.7 GHz

6. Conclusions

This work presents the design and manufacture of a reflectarray (RA) antenna for the Ku-band, based on a fully-metallic 3D architecture. The structure used for the array structure is a FSS based on a fully-metallic design, which consists of a two-dimensional arrangement of classical square waveguides, being each of these waveguides the unit cell of the whole structure. The cell is shorted by placing a ground plane at the bottom, in order to force full-reflection response. Each cell has the ability of configuring the phase of its own reflected field by means of resonators perforated on the walls of the cell waveguide section. These perforations actually play the role of slots resonators, which modify drastically the electromagnetic response of the cell at frequencies close to their own resonance frequency. In this manuscript, two main resonator-shapes are proposed (*C-shaped* and *S-shaped* slot resonators). The inclusion of resonant elements along the propagation direction permits the separate control of the vertical and horizontal field-polarizations. The designed structure proposed in this paper as a proof of concept is focused on the control of the V-pol incidence. This design explores the potential of phase value truncation (6 states and 2 states), and demonstrates that proper pattern results can be obtained with this phase truncation. There is good agreement between the design outcomes and the measurement results of the design.

Acknowledgements

This work was supported in part by the Spanish Government under Project PID2020-112545RB-C54, Project RTI2018-102002-A-I00 and Project TIN2016-75097-P, in part by "Junta de Andalucía" under Project B-TIC-402-UGR18, A-TIC-608-UGR20 and Project P18.RT.4830, and in part by the Project associated with the Leonardo Scholarship 2021 for researchers and cultural creators from the BBVA foundation. The authors would like to thank the constructive comments and help of Prof. Pablo Padilla.

1. A. Gupta and R. K. Jha, "A Survey of 5G Network: Architecture and Emerging Technologies," in IEEE Access, vol. 3, pp. 1206-1232, 2015

2. M. Agiwal, H. Kwon, S. Park and H. Jin, "A Survey on 4G-5G Dual Connectivity: Road to 5G Implementation," in IEEE Access, vol. 9, pp. 16193-16210, 2021
3. M. H. Dahri, M. H. Jamaluddin, M. I. Abbasi and M. R. Kamarudin, "A Review of Wideband Reflectarray Antennas for 5G Communication Systems," in IEEE Access, vol. 5, pp. 17803-17815, 2017, doi: 10.1109/ACCESS.2017.2747844.
4. J. Huang, J. A. Encinar, "Introduction to Reflectarray Antenna," Wiley-IEEE press, 2008
5. T. Katagi and I. Chiba, "Review on recent phased array antenna technologies in Japan," IEEE Antennas and Propagation Society International Symposium. Transmitting Waves of Progress to the Next Millennium. 2000 Digest. Held in conjunction with: USNC/URSI National Radio Science Meeting (C, 2000, pp. 570-573 vol.2
6. S. Samejima, "Phased array antenna systems for commercial applications in Japan," Proceedings of International Symposium on Phased Array Systems and Technology, 1996
7. R. Rotman and M. Tur, "Antenna and beamformer requirements for wideband phased array systems: A review," 2009 IEEE International Conference on Microwaves, Communications, Antennas and Electronics Systems, 2009
8. R. Mailloux, Phased Array Antenna Handbook, Third Edition , Artech, 2017.
9. P. Chen and W. Hong, "Research advances in phased array antennas for satellite communications," 12th European Conference on Antennas and Propagation (EuCAP 2018), 2018
10. A. A. Rauf, J. Tahir, A. Raza, A. Ali and I. H. Umrani, "16 ways X-band wilkinson power divider for phased array transmitter," 2018 15th International Bhurban Conference on Applied Sciences and Technology (IBCAST), 2018, pp. 835-840
11. Q. Zhang, C. Yuan and L. Liu, "Studies on mechanical tunable waveguide phase shifters for phased-array antenna applications," 2016 IEEE International Symposium on Phased Array Systems and Technology (PAST), 2016
12. D. M. Pozar, "The active element pattern," in IEEE Transactions on Antennas and Propagation, vol. 42, no. 8, pp. 1176-1178, Aug. 1994
13. P. Nayeri, J. Yang, A. Z. Elsherbeni, "Reflectarray Antennas: Theory, Designs, and Applications," Wiley-IEEE press, 2018
14. D. Berry, R. Malech and W. Kennedy, "The reflectarray antenna," in IEEE Transactions on Antennas and Propagation, vol. 11, no. 6, pp. 645-651, Nov. 1963
15. J. A. Encinar, "Design of two-layer printed reflectarrays using patches of variable size," in IEEE Transactions on Antennas and Propagation, vol. 49, no. 10, pp. 1403-1410, Oct. 2001
16. M. Arrebola, J. A. Encinar and M. Barba, "Multifed Printed Reflectarray With Three Simultaneous Shaped Beams for LMDS Central Station Antenna," in IEEE Transactions on Antennas and Propagation, vol. 56, no. 6, pp. 1518-1527, June 2008
17. P. Robustillo, J. Zapata, J. A. Encinar and M. Arrebola, "Design of a Contoured-Beam Reflectarray for a EuTELSAT European Coverage Using a Stacked-Patch Element Characterized by an Artificial Neural Network," in IEEE Antennas and Wireless Propagation Letters, vol. 11, pp. 977-980, 2012
18. R. Florencio, J. A. Encinar, R. R. Boix, V. Losada and G. Toso, "Reflectarray Antennas for Dual Polarization and Broadband Telecom Satellite Applications," in IEEE Transactions on Antennas and Propagation, vol. 63, no. 4, pp. 1234-1246, April 2015, doi: 10.1109/TAP.2015.2391279
19. B. Li, C. Y. Mei, Y. Zhou and X. Lv, "A 3-D-Printed Wideband Circularly Polarized Dielectric Reflectarray of Cross-Shaped Element," in IEEE Antennas and Wireless Propagation Letters, vol. 19, no. 10, pp. 1734-1738, Oct. 2020
20. P. Mei, S. Zhang and G. F. Pedersen, "A Low-Cost, High-Efficiency and Full-Metal Reflectarray Antenna With Mechanically 2-D Beam-Steerable Capabilities for 5G Applications," in IEEE Transactions on Antennas and Propagation, vol. 68, no. 10, pp. 6997-7006, Oct. 2020, doi: 10.1109/TAP.2020.2993077.
21. K. Q. Henderson and N. Ghalichechian, "Circular-Polarized Metal-Only Reflectarray With Multi-Slot Elements," in IEEE Transactions on Antennas and Propagation, vol. 68, no. 9, pp. 6695-6703, Sept. 2020
22. R. Deng, F. Yang, S. Xu and M. Li, "A Low-Cost Metal-Only Reflectarray Using Modified Slot-Type Phoenix Element With 360° Phase Coverage," in IEEE Transactions on Antennas and Propagation, vol. 64, no. 4, pp. 1556-1560, April 2016
23. D. Z. Zhu, M. D. Gregory, P. L. Werner and D. H. Werner, "Fabrication and Characterization of Multiband Polarization Independent 3-D-Printed Frequency Selective Structures With UltraWide Fields of View," in IEEE Transactions on Antennas and Propagation, vol. 66, no. 11, pp. 6096-6105, Nov. 2018

24. A. K. Rashid and Z. Shen, "Three-dimensional frequency selective surfaces," 2010 International Conference on Communications, Circuits and Systems (ICCCAS), 2010, pp. 688-691, doi: 10.1109/ICCCAS.2010.5581918.
25. C. Pelletti, G. Bianconi, R. Mittra, and Z Shen, "Frequency selective surface with wideband quasi-elliptical bandpass response," in Electronics Letters, vol. 49, no. 17, pp. 1052-1053, Aug. 2013
26. A. A. Omar and Z. Shen, "Multiband High-Order Bandstop 3-D Frequency-Selective Structures," in IEEE Transactions on Antennas and Propagation, vol. 64, no. 6, pp. 2217-2226, June 2016
27. C. Molero, T. Debogovic and M. García-Vigueras, "Design of Full-Metal Polarizing Screen Based on Circuit Modeling," 2018 IEEE/MTT-S International Microwave Symposium - IMS, 2018, pp. 23-26
28. C. Molero Jimenez, E. Menargues and M. García-Vigueras, "All-Metal 3-D Frequency-Selective Surface With Versatile Dual-Band Polarization Conversion," in IEEE Transactions on Antennas and Propagation, vol. 68, no. 7, pp. 5431-5441, July 2020, doi: 10.1109/TAP.2020.2975270.
29. J. Y. Dai et al., "Wireless Communication Based on Information Metasurfaces," in IEEE Transactions on Microwave Theory and Techniques, vol. 69, no. 3, pp. 1493-1510, March 2021, doi: 10.1109/TMTT.2021.3054662.
30. K. Deb, A. Pratap, S. Agarwal and T. Meyarivan, "A Fast and Elitist Multiobjective Genetic Algorithm: NSGA-II," in IEEE Transactions on Evolutionary Computation, vol. 6, no. 2, pp. 182-197, April 2022, doi: 10.1109/4235.996017.
31. C. Molero, A. Palomares, A. Álex, I. Parellada, F. Gámiz, P. Padilla, J. F. Valenzuela, "Metamaterial-Based Reconfigurable Intelligent Surface: 3D Meta-Atoms Controlled by Graphene Structures," in IEEE Communications Magazine, June 2021, doi: 10.1109/MCOM.001.2001161.

 doi:10.20944/preprints202110.0024.v1